Electronic structure and surface band bending of Sn-doped β-Ga_2O_3 thin films studied by x-ray photoemission spectroscopy and *ab initio* calculations

Jiaye Zhang,[1,*] Zhenni Yang,[1,2,*] Siliang Kuang,[1,2] Ziqi Zhang,[1] Shenglong Wei,[1] Joe Willis,[3,4] Tien-Lin Lee,[4] Piero Mazzolini,[5] Oliver Bierwagen,[6] Shanquan Chen,[7] Zuhuang Chen,[7] Duanyang Chen,[8] Hongji Qi,[2,8,†] David Scanlon,[3,9,‡] and Kelvin H. L. Zhang[1,§]

[1]*State Key Laboratory of Physical Chemistry of Solid Surfaces, College of Chemistry and Chemical Engineering, Xiamen University, Xiamen 361005, People's Republic of China*

[2]*Hangzhou Institute of Optics and Fine Mechanics, Hangzhou 311421, People's Republic of China*

[3]*Department of Chemistry, University College London, 20 Gordon Street, London WC1H 0AJ, United Kingdom and Thomas Young Centre, University College London, Gower Street, London WC1E 6BT, United Kingdom*

[4]*Diamond Light Source Ltd., Harwell Science and Innovation Campus, Didcot OX11 0DE, United Kingdom*

[5]*Department of Mathematical, Physical and Computer Sciences, University of Parma, Parco Area delle Scienze 7/A, Parma 43124, Italy*

[6]*Paul-Drude-Institut für Festkörperelektronik, Leibniz-Institut im Forschungsverbund Berlin e.V., Hausvogteiplatz 5-7, 10117 Berlin, Germany*

[7]*School of Materials Science and Engineering, Harbin Institute of Technology, Shenzhen 518055, People's Republic of China*

[8]*Key Laboratory of Materials for High Power Laser and Research Center of Laser Crystal, Shanghai Institute of Optics and Fine Mechanics, Chinese Academy of Sciences, Shanghai 201800, People's Republic of China*

[9]*School of Chemistry, The University of Birmingham, Edgbaston, Birmingham B15 2TT, United Kingdom*

(Received 3 August 2023; revised 7 May 2024; accepted 14 June 2024; published 11 September 2024)

The bulk and surface electronic structures of Sn-doped β-Ga_2O_3 thin films have been studied by soft and hard x-ray photoemission spectroscopy (soft PES at 1486.6 eV and HAXPES at 5920 eV). The experimental spectra are compared with density functional theory calculated density of states in the valence band and conduction band. Excellent agreement was found between experimental spectra and calculated density of states by taking into account the photoionization cross section of different orbitals involved in the valence and conduction bands. The electronic states derived from Ga 4*s* character are selectively enhanced by HAXPES. This allows us to infer that the states at the conduction band and bottom of the valence band contain pronounced Ga 4*s* character. The occupation of the lower conduction band in degenerately Sn-doped Ga_2O_3 is clearly observed by HAXPES, which allows for direct measurement of Burstein-Moss shift and band-gap renormalization as a function of Sn doping. A comparison of the valence band spectra of Sn-doped Ga_2O_3 films with Si-doped samples suggests that Sn doping has different effects on the electronic structure than Si doping. An in-gap electronic state is observed for Sn-doped Ga_2O_3, which is attributed to self-compensating Sn^{2+} related defects. Furthermore, a larger band-gap renormalization is found in Sn-doped samples, because the Sn 5*s* dopant orbital mixes strongly with the host Ga 4*s* derived conduction band. Finally, a comparison of the valence band and core-level spectra excited with soft and hard x rays allows us to identify an upward band bending at the surface region of Sn-doped Ga_2O_3 films.

DOI: 10.1103/PhysRevB.110.115120

I. INTRODUCTION

Monoclinic β-phase Ga_2O_3 has garnered significant interest as a wide band gap semiconductor for various device applications, including high-power electronics, solar-blind deep ultraviolet (DUV) photodetectors, and DUV transparent conductive oxides (TCOs). This is due to its ultralarge band gap of approximately 4.8 eV, high theoretical breakdown field of 8 MV/cm, controllable *n*-type dopability, and availability of large-scale substrate wafers grown from the melt [1–3]. These advantages offer a competitive edge over current wide band gap semiconductors such as SiC and GaN. In the context of these device applications, the ability to regulate the charge carrier concentrations and defects is of essential importance [4,5]. For instance, in Ga_2O_3 used as an active channel layer in high-power electronics, a low carrier concentration with high mobility is necessary in order to achieve a high breakdown voltage [6]. However, highly conductive Ga_2O_3 with higher carrier concentrations over 10^{19} cm^{-3} is required for Ga_2O_3 used as a DUV transparent conductive electrode and ohmic contact in modulation-doped high-mobility heterostructures [7].

Achieving precise control over carrier concentration and mobility entails incorporating dopants with small activation energies while simultaneously suppressing the formation of compensating defects. Various dopants have been investigated for this purpose, including group IV elements such as Si, Ge, and Sn [8–11], as well as transition metals like Ta, Nb,

*These authors contributed equally to this work.
†Contact author: qhj@siom.ac.cn
‡Contact author: d.scanlon@ucl.ac.uk
§Contact author: Kelvinzhang@xmu.edu.cn

and Zr [12–14], among others. These dopants have been demonstrated to tune carrier concentrations in Ga_2O_3 bulk crystals and thin films within the range of 10^{16}–$10^{20}\,cm^{-3}$. Notably, Sn-doped Ga_2O_3 bulk crystals are commonly utilized as *n*-type substrates [15]. Thin films of Si and Sn-doped Ga_2O_3 have found application as doping layers in different types of field-effect transistors (FETs) and Schottky barrier diodes (SBDs). Heavily Si-doped Ga_2O_3 layers with carrier concentration of $5\times10^{19}\,cm^{-3}$ have been employed as low-resistance ohmic contacts to Ga_2O_3, effectively reducing the parasitic resistance in Ga_2O_3-based high-mobility transistors [7].

On the other hand, doping of semiconductors also alters the optical and electronic structure of the host semiconductor, due to the introduction of additional dopant electronic states and the high density of free electrons [16]. The electronic structure, particularly the energy band dispersion at the conduction band (CB) edge, and its resulting transport properties, are influenced by the electronic states of dopant ions and electron concentrations [17,18]. Therefore, to fully exploit the potential of doped Ga_2O_3 in optoelectronic device applications, it is essential to comprehend the electronic structure of *n*-type doped Ga_2O_3 [19].

The electronic structure of undoped β-Ga_2O_3 has been studied by *ab initio* calculations [20–23], optical spectroscopy [24], and a few photoemission spectroscopy experiments [22,25–29]. There is general consensus that Ga_2O_3 has a direct band gap of ∼4.85 eV and a slightly smaller indirect band gap [20]. Standard density functional theory (DFT) calculations result in an underestimation of the band gap because of the underestimation of the energy position of Ga 3*d* semicore states and the overestimation of Ga 3*d*-O 2*p* hybridization at the top of the valence band (VB) [30]. On the other hand, Heyd-Scuseria-Ernzerhof (HSE06) hybrid functionals [20,23] and the *GW* approximation approach [21,22] have been demonstrated to provide better agreement with experimental band gaps and lattice parameters. The CB of Ga_2O_3 is mainly composed of delocalized Ga 4*s* derived states giving rise to a dispersive CB edge with a low electron effective mass, while the VB is mainly formed by occupied O $2p^6$ derived states with minor hybridization with Ga 3*d*, 4*p*, and 4*s* orbitals. The localized nature of the O 2*p* derived VB edge makes it challenging to achieve reliable *p*-type doping in Ga_2O_3 [5,19]. The VB spectra of undoped Ga_2O_3 have been experimentally measured using photoelectron spectroscopy excited with a range of photon energies [22,25–28], yielding consistent results with the calculated density of states (DOS). However, to date, there has been limited investigation into the impact of *n*-type doping on the electronic structure and defect states of Ga_2O_3.

Additionally, there remains a debate concerning the surface band bending of Ga_2O_3. The works of Navarro-Quezada *et al.* [25,26] and Lovejoy *et al.* [27] reported an upward surface band bending up to 0.5 eV (electron depletion) existing on the Ga_2O_3 (100) surface, as measured by x-ray photoemission spectroscopy (XPS). However, Swallow *et al.* [28] argued that the analysis of XPS VB spectra by linear extrapolation of the VB edge leads to underestimation of the surface valence band maximum (VBM) to the Fermi level; they claimed that the surface band bending is downward (electron accumulation) when considering the instrumental broadening effect accurately. It is important to note that the surface band bending is significantly influenced by the presence of surface adsorbates and the bulk carrier concentration. Recent work by Gazoni *et al.* suggests that removal of the OH termination adsorbed on an as-received Ga_2O_3 ($\bar{2}01$) single-crystal surface produced a large upward shift in band bending of up to 1.0 eV [31].

In this work, we provide an in-depth study of the electronic structure of Sn-doped Ga_2O_3 using photoelectron spectroscopy and HSE06 hybrid functional calculations. We grew Sn-doped Ga_2O_3 homoepitaxial thin films with carrier concentrations from $2.8\times10^{18}\,cm^{-3}$ to $1.3\times10^{20}\,cm^{-3}$ using pulsed laser deposition (PLD). The core levels, VB, and occupied CB spectra were measured by photoelectron spectroscopy excited with soft x rays (soft PES at 1486.6 eV) and hard x rays (HAXPES at 5920 eV). HAXPES enhances the ability to detect the Ga 4*s* orbital because of the increased photoionization cross section for Ga 4*s* relative to O 2*p* [32] and provides an approach to the direct observation of the doped electronic states at the CB. Furthermore, utilizing HAXPES also allows us to obtain true bulk electronic structure of the materials due to the much longer electron mean path length and correspondingly enhanced bulk sensitivity [33]. On the other hand, the soft PES is a more surface sensitive technique, which reflects electronic properties at the surface region. The combination of soft PES and HAXPES allows us to resolve the surface band bending of Ga_2O_3.

II. EXPERIMENT

A. Thin film growth and characterization

Homoepitaxial Sn-doped β-Ga_2O_3 thin films were grown on Fe-doped semi-insulating (010) β-Ga_2O_3 substrates using PLD from respective targets. Sn-doped Ga_2O_3 targets with Sn doping concentrations of $x = 0.01\%$, 0.1%, 1%, and 3% [i.e., mole ratio $x = Sn/(Sn + Ga)$] were made by mixing and grinding the appropriate proportions of Ga_2O_3 (99.999%, Alfa Aesar) and SnO_2 (99.999%, Alfa Aesar) polycrystalline powder, followed by cold pressing and sintering in air at 1350 °C for 24 h. During the growth, laser ablation was performed at an energy density of $1.4\,J/cm^2$. Films were grown at a substrate temperature of 650 °C in 10 mTorr O_2 with a target-substrate distance of 50 mm. In addition, two Si-doped Ga_2O_3 films with Si doping level of 0.5% and 1% were also grown for comparison. Details about the growth of Si-doped Ga_2O_3 can be found in Ref. [34]. All film thickness are ∼200 nm. The crystal structures of thin films were determined by a Rigaku SmartLab high-resolution x-ray diffractometer (XRD), using Cu $K\alpha$ radiation ($\lambda = 0.15406\,nm$) and parallel beam optics.

B. Photoemission spectroscopy

Soft PES measurements were performed on a Thermo Scientific ESCALAB Xi^+ spectrometer using a monochromatized Al $K\alpha$ x-ray source ($h\nu = 1486.6\,eV$). The emitted electrons were detected using a hemispherical analyzer at a normal emission angle (electron takeoff angle = 90° relative to the surface plane) and the total energy resolution was ∼0.50 eV. HAXPES measurements at a photon energy of 5920 eV were conducted at beamline I09, Diamond Light

Source, UK. The end station is equipped with a VG Scienta EW4000 electron analyzer with ±28° angular acceptance. During the measurements, the photon beam is perpendicular to the electron emission direction. The photon beam is polarized in a horizontal plane resulting in the electric vector being aligned with the electron emission direction. The sample was placed in a grazing incidence geometry (∼10°), with the surface normal in the plane defined by the photon beam and electron emission direction, thereby significantly enhancing the count rate. All these samples were prepared by mounting the thin films on copper sample holders with carbon tape and electrical contact was made at the corners of the films to avoid charging effects. The pass energy and step size were set at 200 and 0.05 eV, resulting in an overall energy resolution of ∼0.25 eV. The binding energy scale was calibrated by an Au foil using the Fermi edge cutoff at 0 ± 0.02 eV and Au $4f_{7/2}$ core level at 84.00 ± 0.02 eV.

C. DFT calculations

Density functional theory calculations were performed using the periodic code VASP (version 5.4.4) [35,36], which uses a plane-wave basis set and describes the interactions between valence and core electrons using the projector augmented wave (PAW) method [35,36]. Ga[$3d^{10}4s^24p^1$], Si[$3s^23p^2$], Sn[$4d^{10}5s^25p^2$], and O[$2s^22p^4$] PAW pseudopotentials were chosen for this work. The HSE06 hybrid exchange correlation functional, with an increased Hartree-Fock mixing parameter α of 32%, was used in order to accurately reproduce the bulk band gap and lattice parameters of Ga_2O_3, as has been performed in other computational studies of Ga_2O_3 in the literature [20,23,37]. A plane-wave cutoff of 475 eV and bulk Γ-centered k-point mesh of 8×8×4 were found to converge the total energy to less than 1 meV per atom and accurately describe the electronic structure. While a ten-atom cell was utilized for undoped Ga_2O_3, one Ga atom replaced by Sn and Si in the 80-atom Ga_2O_3 cell was employed to deal with Sn and Si doping, respectively. This corresponds to replacing one dopant atom in 32 Ga atoms, i.e., 3.125% doping and a carrier concentration of 1.2×10^{21} cm^{-3}. These supercells and relevant input files were generated using many of the tools available in the PYCDT package [38]. After relaxation with a Γ-centered 2×2×2 k-point grid, band structures were computed along the high-symmetry path $X \rightarrow N$ in order to capture the behavior at the conduction band minimum. Analysis and plotting of band structures were performed with the SUMO PYTHON package [39]. For the total and projected density of states for undoped and doped supercells, a Gaussian broadening of 0.6 eV and a Lorentzian broadening of 0.2 eV were applied using the GALORE software [40].

III. RESULTS AND DISCUSSION

A. Epitaxial thin films and electrical properties

The monoclinic crystal structure of β-phase Ga_2O_3 [Fig. 1(a)] has two nonequivalent Ga sites, including the tetrahedrally (T_d) coordinated Ga_1 site and octahedrally (O_h) coordinated Ga_2 site. Sn dopants in Ga_2O_3 preferentially substitute Ga at the O_h coordinated Ga_2 site, while Si dopants prefer the T_d coordinated Ga_1 site, because of better

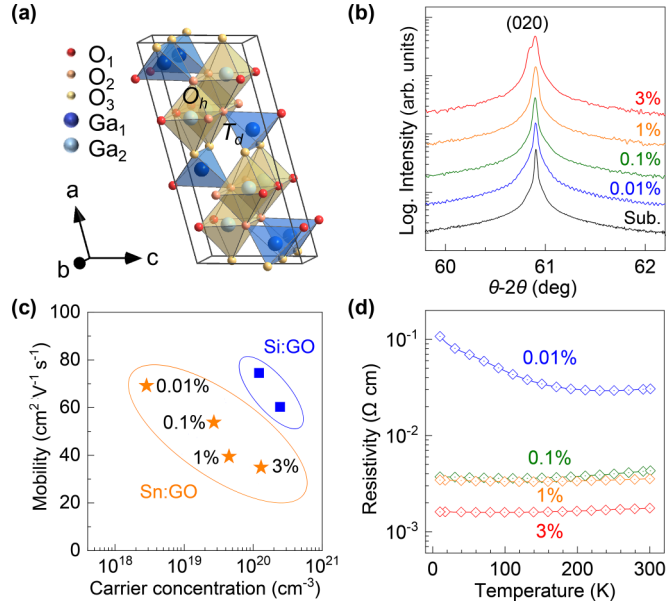

FIG. 1. (a) Crystal structure of monoclinic β-phase Ga_2O_3; Ga_1 and Ga_2 are located at T_d and O_h coordination, respectively. (b) Out of plane θ-2θ XRD pattern at the vicinity of Ga_2O_3 (020) reflection. (c) Room-temperature Hall mobility as a function of carrier concentration for Sn- and Si-doped Ga_2O_3 thin films. (d) Temperature dependence of resistivity for $(Sn_xGa_{1-x})_2O_3$ with different x.

accommodation of the different ionic radii at the respective sites [8]. Figure 1(b) shows θ-2θ XRD patterns around the (020) diffraction peak of Ga_2O_3. When the Sn doping levels x are $\leqslant$1%, the film (020) peaks overlap with that of the substrate, and the films have very similar lattice constants as the bulk Ga_2O_3 (3.037 Å). However, for the $x = 3\%$ Sn-doped films, the out of plane lattice constants are slightly larger than that of the bulk Ga_2O_3 substrate. The increase of lattice constant is due to the ionic radius of Sn^{4+} (0.69 Å) being larger than that of O_h Ga_2 (0.62 Å) [8].

Figure 1(c) and Table I present a summary of the room-temperature carrier concentration (n_e) and mobility (μ) of the Sn-doped films, as well as for 0.5% and 1% Si-doped Ga_2O_3 films. The film with 0.01% Sn doping exhibits the highest mobility of 69 cm^2/V s. As more Sn is doped, the film's mobility decreases due to scattering by the dopants. Films with 1% and 3% Sn doping show higher carrier concentrations of 4.5×10^{19} and 1.3×10^{20} cm^{-3}, respectively, but lower mobilities of 39.5 and 35 cm^2/V s. Interestingly, the

TABLE I. Room-temperature carrier concentration (n_e), mobility (μ), and conductivities (σ) for Sn- and Si-doped Ga_2O_3 thin films on Ga_2O_3 (010) substrates.

Dopant	x	n_e (cm^{-3})	μ (cm^2/V s)	σ (S/cm)
Sn	0.01%	2.8×10^{18}	69.2	30.9
	0.1%	2.7×10^{19}	53.8	232
	1%	4.5×10^{19}	39.5	283
	3%	1.3×10^{20}	34.9	724
Si	0.5%	1.1×10^{20}	75.0	1322
	1%	2.6×10^{20}	60.3	2500

0.5% and 1% Si-doped films exhibit much higher mobilities of 75 and 60.3 $cm^2/V\,s$, respectively, with carrier concentrations of 1.3×10^{20} and $2.6\times10^{20}\,cm^{-3}$, despite the lower Si dopant levels compared to Sn. This indicates that Si is a more efficient *n*-type donor for Ga_2O_3. This result aligns with recent theoretical calculations by Lany [41] and our recent work [42], which suggest that among the group 14 dopants, only Si acts as a truly shallow donor, whereas Sn doping results in a higher donor activation energy and creates defect states close to the conduction band edge.

Figure 1(d) presents the temperature-dependent electrical resistivity (ρ) was measured from 10 to 300 K. The 0.01% Sn-doped film exhibits semiconducting behavior, whereas films with higher Sn levels exhibit characteristics of metallic conductivity, indicating the degenerate doping of Ga_2O_3. Using a static dielectric constant ε_s of 10.2 and electron effective mass (m_0^*) of $0.28m_e$ [43], the effective Bohr radius calculated using $a_B^* = a_H\varepsilon_s/(m_0^*/m_e)$ for a donor state in Ga_2O_3 is approximately 1.9 nm. Consequently, the critical carrier concentration n_c for the onset of degenerate metallic conductivity, as determined by the Mott criterion $(n_c)^{1/3}\,a_B^* \approx 0.25$, is approximately $3\times10^{18}\,cm^{-3}$. The observed trend in transport properties of our films with different Sn doping levels agrees well with the prediction by the Mott criterion for metal-insulator transition.

B. Valence band spectra and electronic structure of Ga_2O_3

The VB and core-level photoemission spectra of the films were excited with soft and hard x rays. Figure 2(a) shows the VB spectra of the 0.01% Sn-doped β-Ga_2O_3 film. We argue that the photoemission spectra of the 0.01% Sn-doped film should closely resemble that of undoped β-Ga_2O_3, given the low Sn doping level and the electron density in the film being below the critical carrier concentration for degenerate doping. Moreover, light Sn doping mitigates the charging effect during photoemission measurements, enabling the referencing of binding energy to the Fermi level (E_F) as zero energy. Therefore, we use the 0.01% Sn-doped film to establish the electronic structure of Ga_2O_3.

The VB spectrum of the 0.01% Sn-doped Ga_2O_3 shown in Fig. 2(a) comprises three main features labeled I–III. The different VB spectral shapes of Ga_2O_3 excited by soft and hard x rays arise from different photoionization cross sections (PICSs) for the orbitals involved in the VB. HSE06 hybrid functional calculations were performed to calculate the electronic structures of Ga_2O_3. The calculated indirect band gap is 4.82 eV, and the lattice parameters are $a = 12.23$ Å, $b = 3.04$ Å, $c = 5.79$ Å, and $\beta = 103.8^\circ$, which are in good agreement with the experimental results [44]. The calculated DOS is depicted in Fig. 2(b) (top), where the VB maximum (VBM) is positioned at 0 eV. The VB primarily consists of filled O $2p^6$ states with small contributions of the Ga 4*s* state near the bottom of the VB, Ga 4*p* in the middle, and Ga 3*d* close to the top of the VB [5,45]. The CB mainly comprises unoccupied Ga 4*s* states.

The calculated one-electron photoionization cross sections for the Ga 4*s*, Ga 4*p*, Ga 3*d*, O 1*s*, and O 2*p* orbitals, taken from the tabulations of Yeh and Lindau [33] are shown in Fig. 2(c). It can be seen that upon increasing the photon

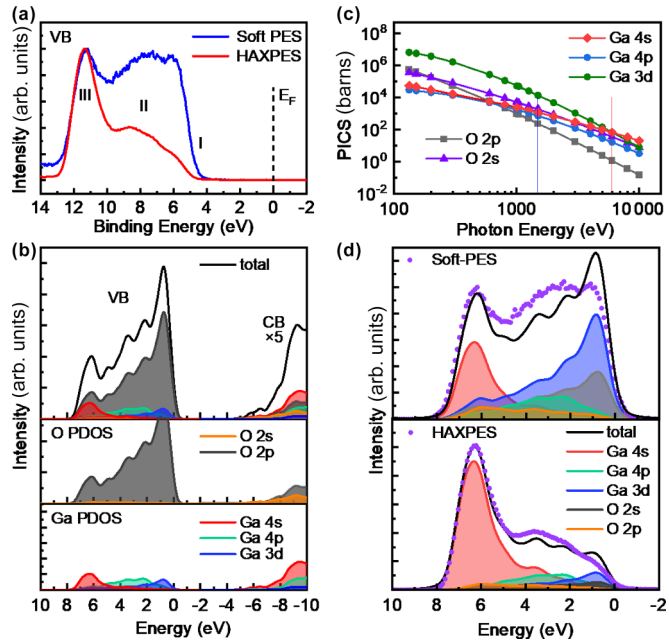

FIG. 2. (a) Soft PES and HAXPES measured valence band spectra of 0.01% Sn-doped Ga_2O_3 sample. (b) DFT-calculated total and partial DOS for Ga_2O_3 around the valence and conduction band, with instrumental (0.6 eV FWHM Gaussian) and lifetime (0.2 eV FWHM Lorentzian) broadening. (c) One-electron photoionization cross sections (PICSs) of Ga 4*s*, Ga 4*p*, Ga 3*d*, and O 2*s*, O 2*p* as a function of photon energy taken from Yeh and Lindau [33] and Scofield [32]. (d) Shirley background subtracted (top) soft PES and (bottom) HAXPES valence band photoemission spectrum of 0.01% Sn-doped Ga_2O_3 sample and the corresponding DFT-calculated total and partial DOS weighted by PICS for Ga_2O_3.The measured valence band photoemission is rigidly shifted to lower energies by 4.95 for soft PES and 5.05 eV for HAXPES to align the VBM at 0 eV binding energy as for the calculation.

energy, the cross sections decrease for all atomic subshells. However, the decrease in intensity for the Ga 4*s*, Ga 4*p*, and Ga 3*d* orbitals is less pronounced than that for the O 2*p* orbital. The relative intensity of states with Ga 4*s*, Ga 4*p*, and Ga 3*d* characters thus shows enhanced intensity at higher photon energies. This is seen in the fact that feature I, which has the most pronounced O 2*p* character, loses most intensity upon increasing the incident photon energy to 5920 eV. Conversely, feature III becomes the dominant feature of the VB spectrum because of the stronger hybridization between the O 2*p* and Ga 4*s* states near the bottom of the VB.

Figure 2(d) presents a comparison between the measured valence band (VB) spectra and the calculated density of states (DOS) for Ga_2O_3. To facilitate a direct comparison between the theoretical and experimental results, the HSE06-calculated DOS were corrected for photoionization cross sections for both soft PES and HAXPES and broadened by a 0.6 eV FWHM Gaussian and a 0.2 eV FWHM Lorentzian accounting for instrument resolution and lifetime broadening to simulate the experimental VB spectra. Both theoretical and experimental VB spectra are aligned to the VBM at 0 eV. The variations in the VB spectral line shapes observed between soft XPS and HAXPES stem from differing orbital contributions weighted by photoionization cross sections. In the soft PES VB spectra,

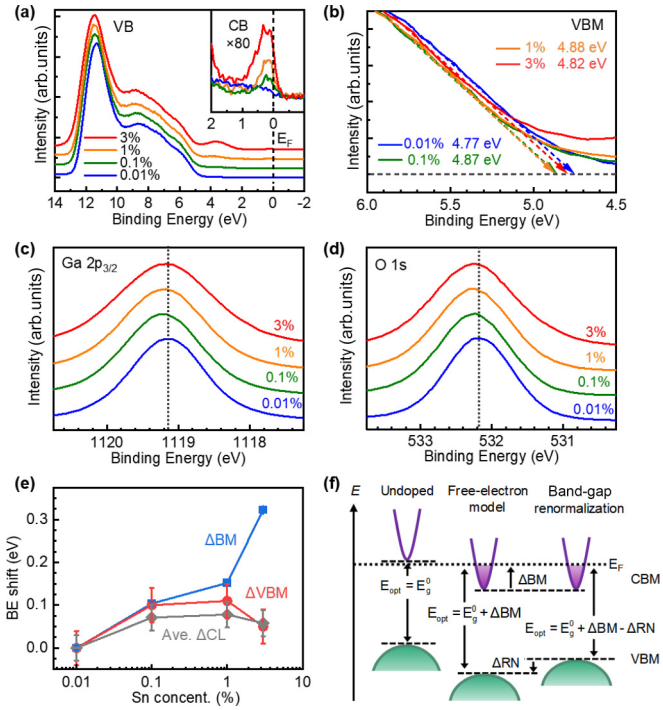

FIG. 3. (a) The HAXPES measured VB structure and expanded view (80×) of the CB state for $(Sn_xGa_{1-x})_2O_3$ with different x. (b) Expanded view of the HAXPES measured VB edges. The HAXPES measured (c) Ga $2p$ and (d) O $1s$ core level for $(Sn_xGa_{1-x})_2O_3$ with different x. (e) The HAXPES measured binding energy (BE) shift of VBM (ΔVBM) and core level (ΔCL) are with resepct to the lowest Sn-doped sample, $x = 0.01\%$. The Burstein-Moss shift (ΔBM) derived from the free-electron model using the n_e determined from Hall measurement. The ΔCL is the average of the shift values for Ga $2p_{3/2}$, O $1s$, Ga $3s$, and Ga $3p$. (f) The schematic diagram for the band structure of the undoped and degenerately doped samples. Doping produces an increase of optical band gap (E_{opt}), consisting of the contributions from the Burstein-Moss shift (ΔBM) and compensating band-gap renormalization (ΔRN); i.e., $\Delta E_{opt} = \Delta BM - \Delta RN$.

the top of the VB is primarily contributed by Ga $3d$ and O $2p$ orbitals because of their large PICs in this excitation energy, while the bottom is mainly influenced by the Ga $4s$ orbital. On the other hand, the HAXPES VB is dominated by the Ga $4s$ feature at the bottom, because of the enhanced crossed section at higher energies. Both the soft PES and HAXPES VB spectral features are fairly well reproduced by the simulations. The good agreement thus validates the HSE06 hybrid functionals for electronic structure calculations of Ga_2O_3 [29]. However, this shows slight disagreement between experimental soft PES VB and simulated VB regarding the relative intensity at the top of the VB [Fig. 2(d), top panel]. This may be induced by the uncertainty in the values of cross sections for Ga $3d$, O $2p$, and Ga $3s$. Nevertheless, there is good agreement for the spectral features in soft PES VB and the simulation.

C. Electronic structure of Sn-doped films

Figure 3(a) displays the HAXPES spectra of Sn-doped β-Ga_2O_3 with different doping levels, encompassing the CB, VB, and band gap regions. For films with Sn doping level $x \geqslant 0.1\%$, CB spectral intensity across the E_F is clearly observed [Fig. 3(a), inset]. According to the calculated DOS, the CB is mainly derived from Ga $4s$ orbital. We assigned the feature near the E_F to the occupied state at the bottom of the CB by doped electrons, consistent with the metallic transport behavior in our films. Richard *et al.* investigated the band structure of a heavily Si-doped Ga_2O_3 single crystal with electron density of $\sim 1\times10^{19}\,cm^{-3}$ using angle-resolved photoemission spectroscopy (ARPES) excited with photon energies ranging from 20 to 40 eV [46]. They also observed a well-defined state across the E_F, which they assigned to the occupied CB by doped electrons, similar to our present work. However, in Richard's work, an occupied state below the E_F was also observed and attributed to the Si impurity state, different from the observation in our work. This discrepancy may arise for their ARPES excited with low photon energies which may provide more surface state, or from the use of different dopants in our studies. On the other hand, for Ga_2O_3 films with Sn doping level less than 0.01%, no appreciable CB feature is observed. This is because the electron density is still lower than the threshold for degenerate doping. Michling and Schmeißer studied the electronic structure of a Ga_2O_3 single crystal with a carrier concentration of $10^{17}\,cm^{-3}$ using resonant photoemission spectroscopy; in this work, no density of states was observed at the E_F, because the Ga_2O_3 single crystal is still in the semiconductor region [47]. As expected, the intensity of the occupied CB feature progressively increases with doping.

With the occupation of the CB bottom, the optical band gap of the Sn-doped Ga_2O_3 should increase, because the CB states are blocked by filled electrons, i.e., Burstein-Moss shift (ΔBM) [48,49]. The corresponding ΔBM based on a free-electron model are summarized in Table II. The values are estimated by the carrier concentration determined from the Hall measurement. For the 0.01% Sn-doped Ga_2O_3, the E_F is located close to the CBM, while for the 3% Sn-doped film with a carrier concentration of $1.3\times10^{20}\,cm^{-3}$, the E_F is positioned at 0.32 ± 0.005 eV above the CBM, i.e., $\Delta BM = 0.32 \pm 0.005$ eV.

The HAXPES measured spectra for the VBM [Fig. 3(b)] and core levels of Ga $2p_{3/2}$ [Fig. 3(c)], O $1s$ [Fig. 3(d)], and Ga $3s$ and Ga $3p$ (see Figs. S1(a) and S1(b) in the Supplemental Material [50]) exhibit slight shifts toward higher binding energy, due to the upward movement of the E_F when the CB is gradually filling with electrons. We determined the VBM positions by linear extrapolation of the leading edge of the VB region to the extended baseline of the VB spectra. This method has been proven to consistently yield correct VBMs with an uncertainty of about ±0.1 eV [51]. The energy range used for the linear fitting is from 5.0 to 6.0 eV, in order to encompass the linear part of the top of the VB. To determine the binding energy shifts of the core levels of Ga $2p_{3/2}$, O $1s$, Ga $3s$, and Ga $3p$, we obtained the energy position of these core levels by measuring the spectral center positions of corresponding peaks after Gaussian and Lorentzian function fitting (details for the fitting and parameters are shown in Fig. S2 and Table S1 in the Supplemental Material [50]). We then used the binding energy shifts of the respective core levels to obtain the average value of core-level shifts. The values of the VBM shifts (ΔVBM) and the average core-level shift

TABLE II. Room-temperature carrier concentration (n_e), the energy separation between the E_F and CBM estimated from the free-electron model (i.e., Burstein-Moss shift, ΔBM), the HAXPES measured VBM values (VBM), the binding-energy shift of HAXPES measured VBM (ΔVBM) and core level (ΔCL), and the band-gap renormalization (ΔRN) derived from the difference between the modeled ΔBM and the HAXPES measured ΔVBM for Sn- and Si-doped Ga_2O_3 thin films. All the binding energy shifts are with respect to the lowest Sn-doped sample, $x = 0.01\%$.

Dopant	x	n_e (cm^{-3})	Modeled ΔBM (eV)	Measured VBM (eV)	Measured ΔVBM (eV)	Measured ΔCL (eV)	Measured ΔRN (eV)
Sn	0.01%	2.8×10^{18}	0	4.77 ± 0.02	0	0	NA
	0.1%	2.7×10^{19}	0.10 ± 0.005	4.87 ± 0.02	0.10 ± 0.04	0.07 ± 0.03	0 ± 0.045
	1%	4.5×10^{19}	0.15 ± 0.005	4.88 ± 0.02	0.11 ± 0.04	0.08 ± 0.03	0.04 ± 0.045
	3%	1.3×10^{20}	0.32 ± 0.005	4.82 ± 0.02	0.05 ± 0.04	0.05 ± 0.03	0.27 ± 0.045
Si	0.5%	1.1×10^{20}	0.29 ± 0.005	4.97 ± 0.02	0.20 ± 0.04	0.18 ± 0.03	0.09 ± 0.045
	1%	2.6×10^{20}	0.49 ± 0.005	4.99 ± 0.02	0.22 ± 0.04	0.24 ± 0.03	0.27 ± 0.045

(ΔCL) with respect to those of 0.01% Sn-doped film are given in Fig. 3(e) and Table II. However, the shifts of the VBMs and core levels (e.g., for 3% Sn-doped sample, $\Delta VBM = 0.05 \pm 0.04$ eV, $\Delta CL = 0.05 \pm 0.04$ eV) are much smaller than the ΔBMs (e.g., 0.32 ± 0.005 eV). This discrepancy is caused by the band-gap renormalization resulting from mutual exchange and Coulomb interactions between the electrons in the CB and electron-dopant interactions [16]. The band-gap renormalization leads to a decrease in the optical band gap. Thus the net change in the optical band gap of a semiconductor of a degenerate semiconductor is affected by the contributions from Burstein-Moss shift (increase) and band-gap renormalization (decrease). The values of the measured band-gap renormalization (ΔRNs) in Table II are derived from the difference between the modeled ΔBM and the measured ΔVBM.

Figure 3(f) displays the schematics for band-gap renormalization in a degenerate semiconductor. The measured energy separation between VBM and E_F (denoted as E_F–VBM) in HAXPES reflects the onset of optical absorption (E_{opt}), and the separation between the VBM and CBM corresponds to the fundamental band gap (E_g^0). Therefore, the measured variation of E_F–VBM (ΔVBM) corresponds to the net change in the optical band gap, while the difference between the shifts of CBM and VBM corresponds to the ΔRN, i.e., $\Delta RN = \Delta CBM - \Delta VBM$. Interestingly, as shown in Table II, the measured ΔVBM and ΔCL for 3% Sn-doped film with respect to those of 0.01% Sn-doped film are found to be much smaller than that of 0.5% Si-doped film ($\sim 0.20 \pm 0.04$ eV) with a similar carrier concentration of $\sim 1.1\times10^{20}$ cm^{-3}. It suggests that the ΔRN is dopant dependent and the Sn and Si doping induces different electronic structures in the host Ga_2O_3. This difference is attributed to the more significant hybridization for the Sn 5*s* than the Si 3*s* dopant state with the CB edge (Ga 4*s*) of Ga_2O_3, which will be further discussed with a combination of DFT results in the following section.

It is interesting to note that an in-gap state centered at the binding energy of ~3.5 eV appears [marked as IGS in Fig. 4(a)] above the VB edge of Sn-doped Ga_2O_3, and the intensity of the in-gap state increases with the Sn doping level. In contrast, the 1% Si-doped Ga_2O_3 film does not show any appreciable intensity for the in-gap state [blue line in Fig. 4(a)], although it has a high carrier concentration of 2.6×10^{20} cm^{-3}. The formation of the pronounced in-gap state at high Sn doping levels may be associated with self-compensating Sn^{2+} valence state related complex defects. The formation of the Sn^{2+} oxidization state may lead to the occupation of the antibonding Sn 5*s*-5*p* hybridized lone pair state above O 2*p*, giving rise to the observed in-gap state. Recent theoretical calculations by Lany [41] reported that Sn is not a truly shallow donor in Ga_2O_3, but has a defect transition energy level $\varepsilon(+/-)$ below the CBM of Ga_2O_3, and therefore the formation of the self-compensating Sn^{2+} oxidization state is favorable when the doping level is high. This situation is very similar to the self-compensation mechanism occurring in Sb-doped SnO_2, in which Sb has a multivalency of Sb^{3+} and Sb^{5+}. Experimental [52] and theoretical studies [18,53] have found that at a low doping level substitutional Sb^{5+} acts as a shallow electron donor, whereas a higher Sb doping level leads to the formation of Sb^{3+} oxidization states which act as electron compensators, limiting the maximum carrier concentration achievable in Sb-doped SnO_2. On the other hand, the

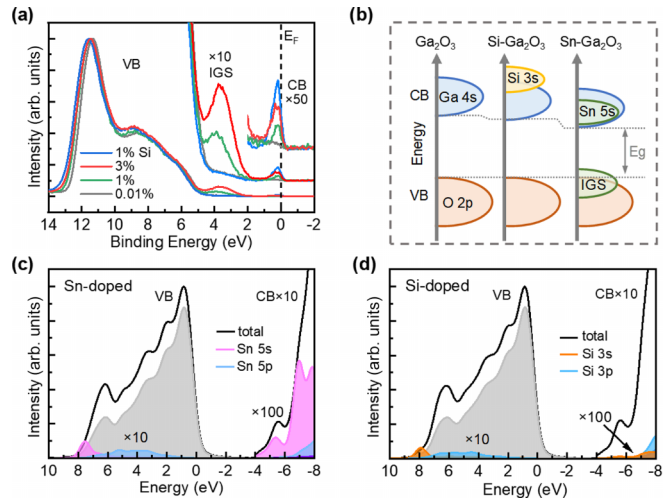

FIG. 4. (a) The HAXPES measured VB and CB structure for $(Sn_xGa_{1-x})_2O_3$ and $(Si_xGa_{1-x})_2O_3$ with different *x*. Inset: expanded view of gap states and CB states close to the Fermi energy (E_F). (b) The diagram of the proposed band edge evolution for undoped Ga_2O_3, and Si-doped Ga_2O_3 and Sn-doped Ga_2O_3. Calculated DOS for (c) Sn- and (d) Si-doped Ga_2O_3. The Sn 5*s*, Sn 5*p*, Si 3*s*, and Si 3*p* partial DOS in VB and CB are multiplied by 10 and 100, respectively; the CB total DOS is multiplied by 10.

Si dopant in Ga_2O_3 is found to have a transition energy level above the CBM and acts as a shallow donor [41]. The different behavior in Si and Sn explains that the carrier concentrations achieved in Si-doped Ga_2O_3 are higher than that of Sn-doped Ga_2O_3, as observed in our films and others reports in the literature [10,11].

Furthermore, because the nuclear charge of Sn is larger than that of Ga, the Sn 5*s* state is expected to be energetically lower than the Ga 4*s* state. We speculated that the bottom of the CB state for Sn-doped Ga_2O_3 has a significant atomic contribution from the Sn dopant [Fig. 4(b)]. To provide atomistic insights into the electronic structure of the doped Ga_2O_3, we turn to DFT calculations. The partial DOS of Sn- and Si-doped Ga_2O_3 are shown in Figs. 4(c) and 4(d), respectively. Due to the Sn 5*s* orbital located at lower energy than the Ga 4*s* orbital, there is a large contribution from the Sn dopant state at the CBM (6.2%), indicating that the Sn state strongly perturbs the CBM of Ga_2O_3. This is in contrast to the situation of Si-doped Ga_2O_3, where the Si state mixes minimally with the CBM. As shown in Fig. 4(d), the Si-doped Ga_2O_3 has a negligible contribution at the CBM (0.8%) and a slightly increased density of Si 3*s* states at around 2 eV above the CBM. Therefore a lower electron effective mass with a more dispersed CB edge, and thus a higher mobility, is expected by the introduction of Si rather than Sn, which is consistent with our experimental results [Fig. 1(d)] and the literature [9,11].

In addition, the different effects of dopants on the host CB structure can explain the different degrees of the band-gap renormalization observed in HAXPES experiments. In the free-electron model mentioned before, we used an electron effective mass of $0.28m_0$ for modeling. However, because of the strong mixing of Sn 5*s* with Ga 4*s*, an increase in band edge effective mass with a less dispersed CB is expected for Sn-doped Ga_2O_3, leading to a smaller ΔBM at a similar carrier concentration. Furthermore, the similar energies of the Ga 4*s* and Sn 5*s* orbitals lead also to greater electron-impurity interaction in Sn-doped Ga_2O_3. Because Sn has a larger nuclear charge than the host Ga cation, Sn doping is expected to result in a greater attractive Coulomb potential around the dopant atoms and further enhance the interaction between the dopant and electrons, leading to larger band-gap renormalization in Sn-doped samples. These two factors together lead to a larger band gap ΔRN for Sn-doped than for Si-doped Ga_2O_3 in the HAXPES spectra. This situation is similar to the different band-gap renormalizations observed in Sn- and Ge-doped In_2O_3 systems [17], where the calculated ΔRN (1.1 eV) for Ge doping is higher than that for Sn doping (0.6 eV) with 10^{21} cm^{-3}. The DFT calculation has demonstrated that this behavior is attributed to the different hybridization of the dopant *s* orbital with the host CB edge: Ge 4*s*, which lies in a lower energy than Sn 5*s*, induces a greater hybridization with the host CB edge and thus more significant lowering and flattening of the CBM, resulting in a higher effective mass of $0.76m_e$ and dopant atom contribution (24%) to the CB than that of Sn-doped systems ($0.43m_e$ and 10%).

D. Surface band bending

The surface electronic properties and surface band bending of Ga_2O_3 are crucial for device performance. The binding energy shift of core levels and VBM derived from photoelectron spectroscopy have been used to determine the surface band bending of semiconductor systems [54]. Figure 5(a) shows a schematic diagram for the probing depths for soft PES ($h\nu$ = 1486.6 eV) and HAXPES ($h\nu$ = 5920 eV), in which the Ga $2p_{3/2}$ photoelectron is used for comparison. The kinetic energy of Ga $2p_{3/2}$ photoelectrons for soft PES is ~360 eV, corresponding to an inelastic mean free path (λ) of 0.8 nm and a probing depth (3λ) of 2.4 nm [33]. For HAXPES, the kinetic energy of Ga $2p_{3/2}$ photoelectrons is 4800 eV, corresponding to an inelastic mean free path of 5 nm and a probing depth of 15 nm. Therefore, the Ga $2p_{3/2}$ from soft PES provides information at the very surface region of the film, whereas the Ga $2p_{3/2}$ from HAXPES provides more information at the bulk of the film.

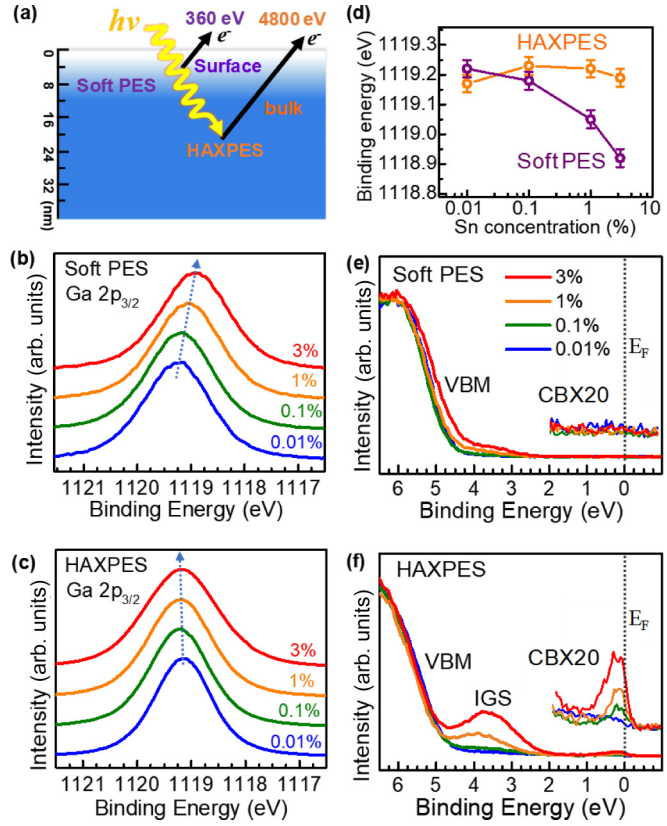

FIG. 5. (a) The schematic diagram of the probing depths for photoelectrons with kinetic energies of 360 and 4800 eV, corresponding to Ga $2p_{3/2}$ excited by soft PES and HAXPES. (b) The soft PES and (c) HAXPES measured Ga $2p_{3/2}$ spectra of $(Sn_xGa_{1-x})_2O_3$ with different Sn concentration. (d) Soft PES and HAXPES measured binding energies Ga $2p_{3/2}$ with different Sn concentration. (e) Soft PES and (f) HAXPES measured VB spectra. Inset: expanded view of CB states (20×) close to the Fermi energy.

Figures 5(b) and 5(c) show the Ga $2p_{3/2}$ spectra of the Sn-doped Ga_2O_3 samples measured by soft PES and HAXPES. In the HAXPES, the Ga $2p_{3/2}$'s slightly shift toward higher binding energy with increasing Sn doping, because of the upshift of the E_F with doped electrons, as discussed in Sec. III C. However, one significant difference for the soft PES is that the Ga $2p_{3/2}$'s gradually shift toward lower binding energies with increasing Sn doping. For example, for the 3% Sn-doped film,

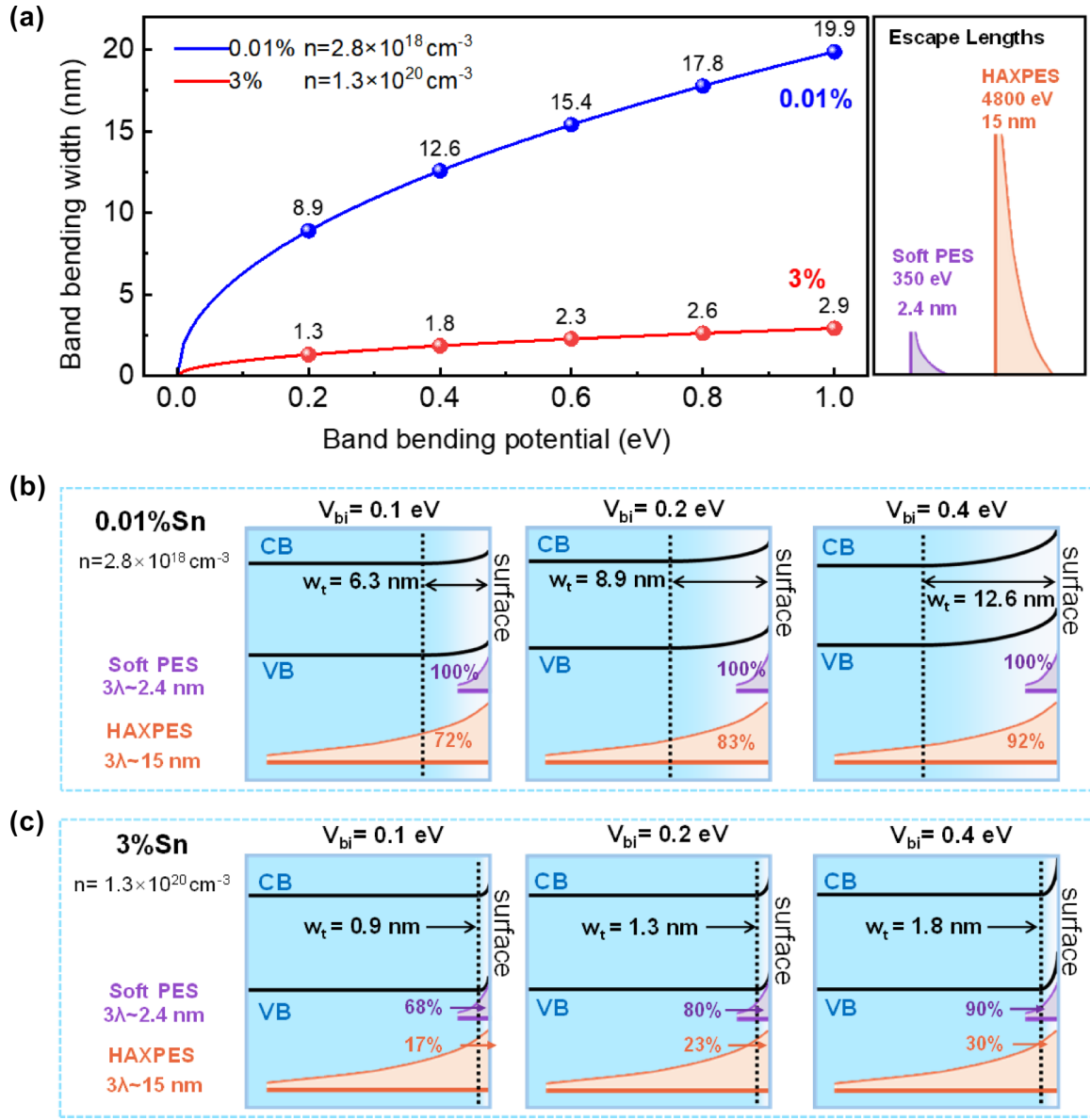

FIG. 6. (a) The band bending widths (W_t) as a function of band bending potentials (V_{bi}) up to 1.0 eV and comparison with escape lengths of Ga $2p_{3/2}$ spectra from soft PES and HAXPES; (b) a schematic diagram of the band bending width of the 0.01% Sn and (c) 3% Sn samples at the band bending potential of 0.1, 0.2 and 0.4 eV compared with the escape length of the Ga $2p_{3/2}$ spectrum of soft PES and HAXPES. The percentage in the figure is the proportion of soft PES or HAXPES signal intensity provided by the band bending region.

the soft PES Ga $2p_{3/2}$'s shift by 0.3 eV toward lower binding energy with respect to the 0.01% Sn-doped sample. The different trend of the shift of Ga $2p_{3/2}$'s measured by soft PES and HAXPES is summarized in Fig. 5(d). The shift of Ga $2p_{3/2}$'s toward lower binding energy in soft PES is in contradiction with the upshift of the E_F in the CB with more Sn doping in Ga_2O_3. Considering the more surface-sensitive character in soft PES and the more bulk-sensitive character in HAXPES, the discrepancy in the binding energy shifts measured by soft PES and HAXPES is an indication of upward surface band bending existing in the surface region of Sn-doped Ga_2O_3. The upward surface band bending is also further evidenced by the comparison of VB spectra from soft PES and HAXPES. As shown in Figs. 5(e) and 5(f), the soft PES VBMs shift toward lower binding energy with increasing Sn doping, while the VBMs measured by HAXPES shift toward higher binding energies. Meanwhile, in the HAXPES VB spectra, a clear density of states is observed at the E_F because of the doped electrons at the bottom of the CB, while no density of states is observed at the E_F for the soft PES VB spectra. This observation suggests a depletion of electrons in the surface region caused by the upward band bending.

Next, we derive the values of surface band bending based on soft PES and HAXPES. We selected the 0.01% and 3% Sn-doped samples to represent cases with lower carrier concentration ($2.8\times10^{18}\,cm^{-3}$) and heavily doped samples ($1.3\times10^{20}\,cm^{-3}$), respectively. Firstly, we calculated the band bending width (W_t) with different bending potentials (V_{bi}) for $2.8\times10^{18}\,cm^{-3}$ and $1.3\times10^{20}\,cm^{-3}$ samples, based on the equation $Wt = \sqrt{2\varepsilon_0\varepsilon_s V_{bi}/qn_e}$, where ε_0 is the vacuum

permittivity, ε_s is the static dielectric constant, $V_{\rm bi}$ is the built-in potential, q is the elementary charge, and n_e is the carrier concentration [54]. Figure 6(a) plots the band bending width for the $2.8\times10^{18}\,\mathrm{cm}^{-3}$ and $1.3\times10^{20}\,\mathrm{cm}^{-3}$ films as a function of band bending potentials from 0 to 1.0 eV. As shown in Fig. 6(b), assuming there are 0.1, 0.2, and 0.4 eV band bending potentials for the $2.8\times10^{18}\,\mathrm{cm}^{-3}$ film, the corresponding band bending widths are calculated to be 6.3, 8.9, and 12.6 nm, respectively. On the other hand, for the $1.3\times10^{20}\,\mathrm{cm}^{-3}$ film [Fig. 6(c)], assuming there are 0.1, 0.2, and 0.4 eV band bending potentials, the corresponding band bending widths are calculated to be 0.9, 1.3, and 1.8 nm, respectively.

Figures 6(b) and 6(c) also compare the probing depths of Ga $2p_{3/2}$ soft PES and HAXPES with the band bending widths with bending potentials of 0.1, 0.2, and 0.4 eV. For the $2.8\times10^{18}\,\mathrm{cm}^{-3}$ sample, because of the larger bending width compared to the probing depth of the soft PES, the Ga $2p_{3/2}$ soft PES can approximately represent the surface, whereas the HAXPES Ga $2p_{3/2}$ can represent the bulk. Furthermore, as shown in Fig. 5(d), for the $2.8\times10^{18}\,\mathrm{cm}^{-3}$ film, the binding energies for the Ga $2p_{3/2}$ from the soft PES and HAXPES are quite similar, indicating there is a very small or negligible surface band bending for the $2.8\times10^{18}\,\mathrm{cm}^{-3}$ film. We also compared binding energies for the VBM positions from soft PES and HAXPES. Both show quite similar values, further confirming very small or negligible surface band bending.

Turning to the $1.3\times10^{20}\,\mathrm{cm}^{-3}$ film, because of the higher carrier concentration, the bandwidth is expected to be narrower than that of the $2.8\times10^{18}\,\mathrm{cm}^{-3}$ film. Figure 6(c) illustrates the comparison of the band bending widths at band bending potentials of 0.1, 0.2, and 0.4 eV with the escape lengths of Ga $2p_{3/2}$ spectra from soft PES and HAXPES. It can be seen that the band bending widths are in the range of 0.9–1.8 nm, comparable to the escape length of soft PES (2.4 nm). On the other hand, the HAXPES is predominated by bulk information. As shown in Figs. 5(b)–5(d), the binding energy of the soft PES Ga $2p_{3/2}$ for the $1.3\times10^{20}\,\mathrm{cm}^{-3}$ sample is located at 1118.92 eV, while the binding energy of the HAXPES is at 1119.19 eV. Considering the soft PES representing for surface and HAXPES for bulk, the binding energy difference suggests there is at least 0.27 eV upward surface band bending. However, as mentioned above, the escape length of Ga $2p_{3/2}$ soft PES is comparable to the band bending width. The soft PES Ga $2p_{3/2}$ is depth integrated spectra in the band bending region. The band bending of 0.27 eV resulting from simply taking the binding energy difference in Ga $2p_{3/2}$ from soft PES and HAXPES would underestimate the band bending value. To derive the band bending value more accurately, we used a model to deconvolute the measured Ga $2p_{3/2}$ spectrum into several spectra at different depth points, taking into account both the surface band bending potential and the escape probability of photoelectrons at different surface layers. This method has been applied for determining the surface band bending of GaN [55,56]. The intensity of the core-level XPS spectrum can be given by the equation $\mathrm{I}(E) = \int_0^d I_0[E(z), z]\exp(-z/\lambda)dz$, where z is the depth from the Ga_2O_3 surface, $I_0[E(z),\ z]$ refers to the contribution from different depths, and λ corresponds to the escape depth of the photoelectron at different depths. We used a 0.5 nm depth step

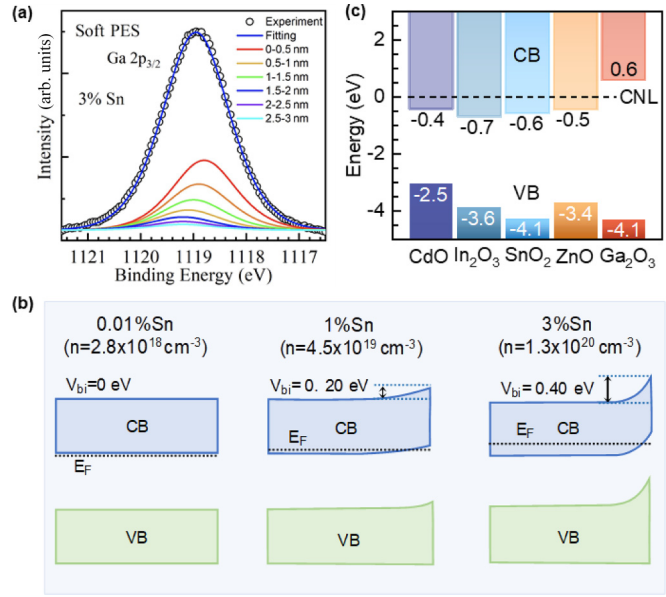

FIG. 7. (a) Fitting diagram of surface energy band bending of the 3% Sn-doped Ga_2O_3. (b) The schematic diagram for surface band bending ($V_{\rm bi}$) of the 0.01%, 1%, and 3% Sn-doped Ga_2O_3. (c) Band line-up with respect to the charge neutrality level (CNL) for Ga_2O_3 and other oxide semiconductors including CdO, In_2O_3, SnO_2, and ZnO. The CNLs of all materials are aligned to 0 eV.

and XPS peaks with full width at half maximum (FWHM) of 1.4 eV to deconvolute the Ga $2p_{3/2}$. The reason to use a FWHM of 1.4 eV is that for the $2.8\times10^{18}\,\mathrm{cm}^{-3}$ film in which there is no detectable surface band banding, the soft PES measured FWHM of the Ga $2p_{3/2}$ is 1.4 eV, and therefore we chose this spectrum as reference. Figure 7(a) shows the deconvolution and fitting result for the soft PES Ga $2p_{3/2}$ spectrum. Therefore, based on the deconvoluted soft PES Ga $2p_{3/2}$ and HAXPES, we can infer that the band bending value for the $1.3\times10^{20}\,\mathrm{cm}^{-3}$ sample is 0.4 eV. Using the same approach, we derived the band bending for the $4.5\times10^{19}\,\mathrm{cm}^{-3}$ sample to be 0.2 eV. Figure 7(b) displays the schematic energy diagrams for the surface band bending for the Sn-doped samples with different carrier concentrations.

Our observation of upward surface band bending is consistent with the results reported by Lovejoy *et al.* [27] and Navarro-Quezada *et al.* [25,26] based on Ga_2O_3 (100) oriented single crystals, and recent results by Gazoni *et al.* [31] based on Ga_2O_3 ($\bar{2}01$) single crystals. On the other hand, Swallow *et al.* [28] questioned the standard method of linear extrapolation of the VB edge of Ga_2O_3 to determine the VBM used in Refs. [25,57], and argued that the linear extrapolation method causes an underestimation of the VBM by ~0.5 eV, resulting from instrumental broadening. Instead, they proposed that there is a 0.24 eV downward band bending at the uncleaned Ga_2O_3 ($\bar{2}01$) surface terminated with hydrogen which produces surface donor states; once the hydrogen is removed by vacuum annealing, an upward band bending of ~0.5 eV relative to the uncleaned surface was observed. In our analysis, the uncertainty arising from instrumental broadening is largely minimized, which can provide more accurate values for the band bending.

The upward band bending in the surface region of Ga_2O_3 is different from the conventional oxide semiconductors, such as In_2O_3 [58–61], SnO_2 [62,63], and ZnO [64], which exhibit a downward band bending and surface electron accumulation at the surface. The general tendency of surface band bending for a semiconductor can be explained within the context of the charge neutrality level (CNL). The energy position of CNL relative to the E_F is the demarcation for a surface state being donorlike (higher than E_F) or acceptorlike (lower than E_F). The energy level of the Ga 4*s* orbital is much higher than those of the In 5*s* and Sn 5*s* orbitals. As seen in Fig. 7(c), the calculated CNL lies nearly 0.6 eV [28] below the CBM in Ga_2O_3, while the CNLs for In_2O_3 [61], SnO_2 [62], and ZnO [64] are located at 0.7, 0.6, and 0.5 eV above the CBM, respectively. In this context, the surface states for those *n*-type Ga-based semiconductors are expected to be "naturally" acceptorlike and their surfaces tend to form electron depletion and upward band bending. Further increase in the doping level will increase the separation between E_F and CNL, giving rise to larger surface upward band bending, which can explain the enhanced upward surface band bending of the Sn-doped Ga_2O_3 thin films at higher carrier concentrations. The upward band bending also induces an electron depletion layer at the surface of Sn-doped Ga_2O_3.

IV. CONCLUSIONS

In summary, a combination of soft and hard x-ray photoemission spectroscopy and density functional theory has been used to study the bulk and surface electronic structures of Sn-doped Ga_2O_3 thin films. Excellent agreement was found between the experimental valence band spectra and calculated density of states for lightly doped Ga_2O_3 by taking into account the photoionization cross section of different orbitals. It has been found that the electronic states at the conduction band and bottom of the valence band are selectively enhanced in HAXPES relative to soft PES. This is attributed to the fact that these states have substantial Ga 4*s* character. With increasing Sn doping in Ga_2O_3, the occupation of the lower conduction band is clearly observed by HAXPES, which allows for the direct determination of band-gap renormalization as a function of Sn doping. Relatively larger band-gap renormalization was found in Sn-doped Ga_2O_3 films in comparison with Si-doped Ga_2O_3 samples, because the Sn 5*s* state mixes strongly with the host Ga 4*s* derived conduction band, as further proved by theoretical calculation. Furthermore, an in-gap state is observed for Sn-doped Ga_2O_3, which is attributed to self-compensating Sn^{2+} related defect states. Insights in electronic structures of Sn-doped Ga_2O_3 may explain the higher activation energy and lower electron mobility observed in Sn-doped Ga_2O_3 films in the literature. Finally, a comparison of the valence band and core-level spectra excited with soft and hard x rays allows us to identify the existing upward surface band bending in the Sn-doped Ga_2O_3.

ACKNOWLEDGMENTS

The authors acknowledge funding support from National Key R&D Program of China (Grant No. 2022YFB3605501) and National Natural Science Foundation of China (Grant No. 22275154). J.W. and D.S. acknowledge Diamond Light Source for cosponsorship of an EngD studentship on the EPSRC Centre for Doctoral Training in Molecular Modelling and Materials Science (EP/L015862/1). D.S. acknowledges support for EPSRC (Grant No. EP/N01572X/1). This work used the ARCHER and ARCHER2 UK National Supercomputing Service, via our membership in the UK's HEC Materials Chemistry Consortium, which is funded by EPSRC (Grants No. EP/L000202, No. EP/R029431, and No. EP/T022213). We are grateful to the UK Materials and Molecular Modelling Hub for computational resources (Thomas and Young), which is partially funded by EPSRC (EP/P020194/1 and EP/T022213/1). The authors acknowledge the use of the UCL Myriad, Kathleen, and Thomas High Performance Computing Facilities (Myriad@UCL, Kathleen@UCL, Thomas@UCL), and associated support services, in the completion of this work. Work by P.M. and O.B. was performed in the framework of GraFOx, a Leibniz-ScienceCampus partially funded by the Leibniz association. We are grateful to the Diamond Light Source for access to beamline I09 under Proposals No. SI31069 and No. SI31681.

[1] M. Higashiwaki, K. Sasaki, A. Kuramata, T. Masui, and S. Yamakoshi, Phys. Status Solidi A **211**, 21 (2014).
[2] S. J. Pearton, J. Yang, P. H. Cary, F. Ren, J. Kim, M. J. Tadjer, and M. A. Mastro, Appl. Phys. Rev. **5**, 011301 (2018).
[3] A. J. Green, J. Speck, G. Xing, P. Moens, F. Allerstam, K. Gumaelius, T. Neyer, A. Arias-Purdue, V. Mehrotra, A. Kuramata *et al.*, APL Mater. **10**, 029201 (2022).
[4] J. Y. Tsao, S. Chowdhury, M. A. Hollis, D. Jena, N. M. Johnson, K. A. Jones, R. J. Kaplar, S. Rajan, C. G. Van de Walle, E. Bellotti *et al.*, Adv. Electron. Mater. **4**, 1600501 (2018).
[5] J. Shi, J. Zhang, L. Yang, M. Qu, D. C. Qi, and K. H. L. Zhang, Adv. Mater. **33**, e2006230 (2021).
[6] A. T. Neal, S. Mou, R. Lopez, J. V. Li, D. B. Thomson, K. D. Chabak, and G. H. Jessen, Sci. Rep. **7**, 13218 (2017).
[7] Y. Zhang, C. Joishi, Z. Xia, M. Brenner, S. Lodha, and S. Rajan, Appl. Phys. Lett. **112**, 233503 (2018).
[8] E. G. Víllora, K. Shimamura, Y. Yoshikawa, T. Ujiie, and K. Aoki, Appl. Phys. Lett. **92**, 202120 (2008).
[9] H. M. Jeon, K. D. Leedy, D. C. Look, C. S. Chang, and D. A. Muller, APL Mater. **9**, 101105 (2021).
[10] E. Ahmadi, O. S. Koksaldi, S. W. Kaun, Y. Oshima, D. B. Short, U. K. Mishra, and J. S. Speck, Appl. Phys. Express **10**, 041102 (2017).
[11] A. Mauze, Y. Zhang, T. Itoh, E. Ahmadi, and J. S. Speck, Appl. Phys. Lett. **117**, 222102 (2020).
[12] H. Cui, H. F. Mohamed, C. Xia, Q. Sai, W. Zhou, H. Qi, J. Zhao, J. Si, and X. Ji, J. Alloys Compd. **788**, 925 (2019).
[13] W. Zhou, C. Xia, Q. Sai, and H. Zhang, Appl. Phys. Lett. **111**, 242103 (2017).

[14] M. Saleh, A. Bhattacharyya, J. B. Varley, S. Swain, J. Jesenovec, S. Krishnamoorthy, and K. Lynn, Appl. Phys. Express **12**, 085502 (2019).

[15] A. Kuramata, K. Koshi, S. Watanabe, Y. Yamaoka, T. Masui, and S. Yamakoshi, Jpn. J. Appl. Phys. **55**, 1202a2 (2016).

[16] K. F. Berggren and B. E. Sernelius, Phys. Rev. B **24**, 1971 (1981).

[17] A. Walsh, J. L. F. Da Silva, and S.-H. Wei, Phys. Rev. B **78**, 075211 (2008).

[18] B. A. D. Williamson, T. J. Featherstone, S. S. Sathasivam, J. E. N. Swallow, H. Shiel, L. A. H. Jones, M. J. Smiles, A. Regoutz, T. L. Lee, X. Xia *et al.*, Chem. Mater. **32**, 1964 (2020).

[19] S. B. Zhang, S. H. Wei, and A. Zunger, Phys. B (Amsterdam) **273-274**, 976 (1999).

[20] J. B. Varley, J. R. Weber, A. Janotti, and C. G. Van de Walle, Appl. Phys. Lett. **97**, 142106 (2010).

[21] J. Furthmüller and F. Bechstedt, Phys. Rev. B **93**, 115204 (2016).

[22] G.-L. Li, F. Zhang, Y.-T. Cui, H. Oji, J.-Y. Son, and Q. Guo, Appl. Phys. Lett. **107**, 022109 (2015).

[23] P. Deák, Q. Duy Ho, F. Seemann, B. Aradi, M. Lorke, and T. Frauenheim, Phys. Rev. B **95**, 075208 (2017).

[24] N. Ueda, H. Hosono, R. Waseda, and H. Kawazoe, Appl. Phys. Lett. **71**, 933 (1997).

[25] A. Navarro-Quezada, S. Alamé, N. Esser, J. Furthmüller, F. Bechstedt, Z. Galazka, D. Skuridina, and P. Vogt, Phys. Rev. B **92**, 195306 (2015).

[26] A. Navarro-Quezada, Z. Galazka, S. Alamé, D. Skuridina, P. Vogt, and N. Esser, Appl. Surf. Sci. **349**, 368 (2015).

[27] T. C. Lovejoy, R. Chen, X. Zheng, E. G. Villora, K. Shimamura, H. Yoshikawa, Y. Yamashita, S. Ueda, K. Kobayashi, S. T. Dunham *et al.*, Appl. Phys. Lett. **100**, 181602 (2012).

[28] J. E. N. Swallow, J. B. Varley, L. A. H. Jones, J. T. Gibbon, L. F. J. Piper, V. R. Dhanak, and T. D. Veal, APL Mater. **7**, 022528 (2019).

[29] J. E. N. Swallow, C. Vorwerk, P. Mazzolini, P. Vogt, O. Bierwagen, A. Karg, M. Eickhoff, J. Schörmann, M. R. Wagner, J. W. Roberts *et al.*, Chem. Mater. **32**, 8460 (2020).

[30] Y. Kang, G. Kang, H.-H. Nahm, S.-H. Cho, Y. S. Park, and S. Han, Phys. Rev. B **89**, 165130 (2014).

[31] R. M. Gazoni, L. Carroll, J. I. Scott, S. Astley, D. A. Evans, A. J. Downard, R. J. Reeves, and M. W. Allen, Phys. Rev. B **102**, 035304 (2020).

[32] J. H. Scofield, Lawrence Livermore Laboratory Technical Report No. UCRL-51326, Lawrence Livermore Laboratory (1973).

[33] J. J. Yeh and I. Lindau, At. Data Nucl. Data Tables **32**, 1 (1985).

[34] J. Zhang, J. Willis, Z. Yang, X. Lian, W. Chen, L.-S. Wang, X. Xu, T.-L. Lee, L. Chen, O. D. Scanlon *et al.*, Cell Rep. Phys. Sci. **3**, 100801 (2022).

[35] G. Kresse and J. Furthmuller, Phys. Rev. B **54**, 11169 (1996).

[36] G. Kresse and J. Hafner, Phys. Rev. B **47**, 558 (1993).

[37] H. Peelaers and C. G. Van de Walle, Phys. Status Solidi B **252**, 828 (2015).

[38] D. Broberg, B. Medasani, N. E. R. Zimmermann, G. Yu, A. Canning, M. Haranczyk, M. Asta, and G. Hautier, Comput. Phys. Commun. **226**, 165 (2018).

[39] A. M. Ganose, A. J. Jackson, and D. O. Scanlon, J. Open Source Software **3**, 717 (2018).

[40] A. J. Jackson, A. M. Ganose, A. Regoutz, R. G. Egdell, and D. O. Scanlon, J. Open Source Software **3**, 773 (2018).

[41] S. Lany, APL Mater. **6**, 046103 (2018).

[42] J. Zhang, J. Willis, Z. Yang, Z. Sheng, L.-S. Wang, T.-L. Lee, L. Chen, D. O. Scanlon, and K. H. L. Zhang, Phys. Rev. B **106**, 205305 (2022).

[43] M. Mohamed, C. Janowitz, I. Unger, R. Manzke, Z. Galazka, R. Uecker, R. Fornari, J. R. Weber, J. B. Varley, and C. G. Van de Walle, Appl. Phys. Lett. **97**, 211903 (2010).

[44] S. Geller, J. Chem. Phys. **33**, 676 (1960).

[45] J. Zhang, J. Shi, D.-C. Qi, L. Chen, and K. H. L. Zhang, APL Mater. **8**, 020906 (2020).

[46] P. Richard, T. Sato, S. Souma, K. Nakayama, H. Liu, K. Iwaya, T. Hitosugi, H. Aida, H. Ding, and T. Takahashi, Appl. Phys. Lett. **101**, 232105 (2012).

[47] M. Michling and D. Schmeißer, IOP Conf. Ser.: Mater. Sci. Eng. **34**, 012002 (2012).

[48] E. Burstein, Phys. Rev. **93**, 632 (1954).

[49] T. S. Moss, Proc. Phys. Soc. London, Sect. B **67**, 775 (1954).

[50] See Supplemental Material at http://link.aps.org/supplemental/10.1103/PhysRevB.110.115120 for additional details on the experimental data processing.

[51] S. A. Chambers, T. Droubay, T. C. Kaspar, and M. Gutowski, J. Vac. Sci. Technol. B **22**, 2205 (2004).

[52] R. F. Martinez-Gazoni, M. W. Allen, and R. J. Reeves, Phys. Rev. B **98**, 155308 (2018).

[53] H. Peng, J. D. Perkins, and S. Lany, Chem. Mater. **26**, 4876 (2014).

[54] S. A. Chambers, L. Wang, and D. R. Baer, J. Vac. Sci. Technol. A **38**, 061201 (2020).

[55] Y. Zhao, H. Gao, R. Huang, Z. Huang, F. Li, J. Feng, Q. Sun, A. Dingsun, and H. Yang, Sci. Rep. **9**, 16969 (2019).

[56] Z. Huang, Y. Wu, Y. Zhao, L. Shi, R. Huang, F. Li, T. Liu, L. Xu, H. Gao, Y. Zhou *et al.*, AIP Adv. **9**, 115106 (2019).

[57] T. Kamimura, K. Sasaki, M. H. Wong, D. Krishnamurthy, A. Kuramata, T. Masui, S. Yamakoshi, and M. Higashiwaki, Appl. Phys. Lett. **104**, 192104 (2014).

[58] K. H. L. Zhang, R. G. Egdell, F. Offi, S. Iacobucci, L. Petaccia, S. Gorovikov, and P. D. C. King, Phys. Rev. Lett. **110**, 056803 (2013).

[59] D. W. Davies, A. Walsh, J. J. Mudd, C. F. McConville, A. Regoutz, J. M. Kahk, D. J. Payne, V. R. Dhanak, D. Hesp, K. Pussi *et al.*, J. Phys. Chem. C **123**, 1700 (2018).

[60] T. Nagata, O. Bierwagen, Z. Galazka, M. Imura, S. Ueda, Y. Yamashita, and T. Chikyow, Jpn. J. Appl. Phys. **58**, SDDG06 (2019).

[61] P. D. C. King, T. D. Veal, D. J. Payne, A. Bourlange, R. G. Egdell, and C. F. McConville, Phys. Rev. Lett. **101**, 116808 (2008).

[62] S. K. Vasheghani Farahani, T. D. Veal, J. J. Mudd, D. O. Scanlon, G. W. Watson, O. Bierwagen, M. E. White, J. S. Speck, and C. F. McConville, Phys. Rev. B **90**, 155413 (2014).

[63] T. Nagata, O. Bierwagen, M. E. White, M. Y. Tsai, Y. Yamashita, H. Yoshikawa, N. Ohashi, K. Kobayashi, T. Chikyow, and J. S. Speck, Appl. Phys. Lett. **98**, 232107 (2011).

[64] R. Heinhold, G. T. Williams, S. P. Cooil, D. A. Evans, and M. W. Allen, Phys. Rev. B **88**, 235315 (2013).